## Title
Changes in Seismic Anisotropy Shed Light on the Nature of the Gutenberg Discontinuity



## Authors
Beghein, Caroline
Yuan, Kaiqing
Schmerr, Nicholas
et al.

## Publication Date
2014-03-14

## DOI
10.1126/science.1246724

Peer reviewed

# Changes in seismic anisotropy shed light on the nature of the Gutenberg discontinuity

Caroline Beghein[1*], Kaiqing Yuan[1], Nicholas Schmerr[2], Zheng Xing[1]
[1]Department of Earth, Planetary, and Space Sciences, University of California, Los Angeles, 595 Charles Young Drive East, Box 951567, Los Angeles, CA 90095-1567
[2]University of Maryland, Department of Geology, College Park, MD 20742

[*]To whom correspondence should be addressed; E-mail: cbeghein@ucla.edu

**Abstract:**

The boundary between the lithosphere and asthenosphere is associated with a plate-wide high seismic velocity "lid" overlying lowered velocities, consistent with thermal models. Seismic body waves also intermittently detect a sharp velocity reduction at similar depths, the Gutenberg (G) discontinuity, which cannot be explained by temperature alone. We compared an anisotropic tomography model with detections of the G to evaluate their context and relation to the lithosphere-asthenosphere boundary (LAB). We find that the G is primarily associated with vertical changes in azimuthal anisotropy and lies above a thermally controlled LAB, implying the two are not equivalent interfaces. The origin of the G is a result of frozen-in lithospheric structures, regional compositional variations of the mantle, or dynamically perturbed LAB.

Plate tectonic theory describes a strong and rigid lithospheric lid that translates coherently atop a weaker and more deformable convecting asthenosphere. Determining the depth and pervasiveness of the interface between these two layers, known as the lithosphere-asthenosphere boundary (LAB), is key for understanding the formation, evolution, and thermochemical properties of plates and associated tectonics. The exact compositional and thermal mechanisms that control this rheological division remain enigmatic, but seismological imaging of anisotropy — the directional dependence of seismic wave velocity — across the upper mantle provides an essential tool for interrogating the transition in material properties across the LAB.

Seismological interrogations of the oceanic upper mantle beneath the Pacific ocean find evidence for a sharp drop in seismic velocity, known as the Gutenberg (G) discontinuity (*1*), at 40–100 km depth. The depth of the G roughly coincides with the top of a low velocity zone (LVZ) and may be the seismological expression of the LAB. However, correlating G depth with plate age and distance to mid-ocean ridges have not produced a unifying interpretation of the relationship between the G and the LAB (*2-6*). This has led to several alternative hypotheses for the origin of the G, including partial melt lenses in the asthenosphere (*3*), hydrogen depletion of olivine from decompression melting beneath mid-oceanic ridges (*7, 8*), frequency dependent attenuation effects reducing the shear modulus in the presence of mantle hydration (*9*), and dynamical melt-producing processes to explain the strong regional variations in G reflectivity from SS precursor data (*5, 10*).

To improve our understanding of how isotropic and anisotropic velocity models relate to the observations of seismic discontinuities, we modeled the three-dimensional (3-D) isotropic and anisotropic structure of the upper mantle beneath the Pacific Basin (Fig. 1) using a global dataset of surface wave phase velocity maps (*11, 12*). The dispersive properties of surface waves make them ideal to put depth constraints on seismic anisotropy and velocity, and the use of higher mode surface waves to model azimuthal anisotropy provides sensitivity throughout the upper mantle (Fig. S1). The detection of changes in seismic anisotropy has been successfully used to identify layering in the mantle, variations in LAB depth beneath continents and oceans (*13, 14*), and chemical stratification within the lithosphere under the North American craton (*14*). Here

we focus on anisotropy under the Pacific plate, which is well sampled by surface waves, and therefore constitutes a natural laboratory to constrain the evolution and cooling history of the oceanic lithosphere. The surface wave anisotropy results are compared to a large dataset of high frequency SS precursors that highlight the G (*5*).

Our models show a stratified upper mantle under the Pacific Ocean, and a correlation between the boundaries of these layers and the location of observed seismic discontinuities (Fig. 2). The top layer (layer 1) is defined by a poor alignment between $V_{SV}$ fast axes direction and the absolute plate motion (APM) (*15*), and the underlying layer (layer 2) by a better alignment with the APM. Layer 1 is also characterized by high seismic velocities away from ocean ridges [4-5% with respect to our reference model (*16*)], and its thickness increases with crustal age, similar to past surface wave studies (*13, 17-19*). Furthermore, layer 1 is associated with 1-2% radial anisotropy with $V_{SV} > V_{SH}$, and azimuthal anisotropy amplitudes of 1-2%. This fast $V_{SV}$ direction roughly follows the orientation of ocean floor fractures zones at 50 km depth near ridges, around 80 km depth for ocean ages between 80 Ma and 120 Ma, and at 100 km depth under old oceanic plates (Fig. 1). Ocean floor fracture zones are temporally stable features that record plate motion path and can thus be used as proxy for the paleospeading directions. Layer 2 has lower S-wave velocity (-5% relative perturbations), strong radial anisotropy (5%) with $V_{SH} > V_{SV}$, and 3% azimuthal anisotropy with, by definition, fast axes sub-parallel to the APM (< 30° deviation from APM).

Based on the above seismological observations, we define the LAB in our models as the dipping interface between these two layers. The strong anisotropy of layer 2 suggests alignment of olivine fast axes with mantle flow direction associated with plate motion, that can occur in the deformable asthenosphere by dislocation creep (*20*) or diffusion creep (*21*). Olivine LPO formed by mantle flow-induced shear strain in the dislocation creep regime is consistent with a low viscosity asthenosphere (*22*) and a flow channel coincident with a low velocity zone (*23*). The thickness of our tomographically defined layer 1 increases with plate age, following the 900ºC–1100ºC isotherms in a HSC model (black lines, Fig. 2). Combined with elevated seismic velocities, layer 1 is therefore consistent with cold lithosphere that has a thermally controlled thickness and implies the LAB is a temperature-related phenomenon. Furthermore, the alignment of the

$V_{SV}$ fast axes with the fossil spreading direction in layer 1 is consistent with LPO and the frozen-in record of past deformation in that layer for ages up to 80 Ma (*13, 19, 21*). For older ages, the fast axes align with the seafloor fracture zones below 50-80 km depth, but they do not align with either the APM or the fossil spreading directions at shallower depths, implying that another mechanism is required to explain the observations in this depth and age range. Note that the depth of the change in radial anisotropy from $V_{SV}>V_{SH}$ to $V_{SH}>V_{SV}$ does not display any age dependence (Fig. 2E), similar to previous observations (*18*), however, synthetic tests and calculation of the resolution matrix revealed the vertical resolution of radial anisotropy models is poor (Figs. S3 and S5).

Of particular interest are the vertical changes in the fast direction of azimuthal anisotropy detected by surface waves beneath the Pacific that overlap with the location of SS precursor detections (*5*) of seismic discontinuities (Fig. 2). For younger crustal ages (< 30 Ma), detections of the G reside at 50-55 km depth, falling above the weaker gradient in azimuthal anisotropy fast axes orientation arising from nearly parallel APM and fossil spreading directions. We caution that resolving the details of the G at depths < 50 km is challenging for the SS precursor technique, this owes to the masking of shallower complexities by the large negative sidelobe of SS (*4*). In addition, ridges are relatively narrow structures compared to the long wavelength SS Fresnel zone (>1000 km) and aliasing of small small-scale structure may occur across the ridge axis. Nonetheless, G detections near the ridges fall within layer 2. For crustal ages between 30 Ma and 100 Ma, G detections coincide with both the depth of a strong change in azimuthal anisotropy and fast axes directions (Figs. 2A, 2C), and lying near the base of layer 1 (55-70 km). Beneath 100-130 Ma crust, the G detections are still associated with the strong gradient in azimuthal anisotropy fast axes direction, primarily falling beneath Hawaii at 75-80 km depth and are confined to the interior of layer 1. The G is poorly resolved beneath regions of crust older than 130 Ma; these regions are undersampled by the SS precursors, with only a few sporadic detections of reflectors beneath the oldest portions of the oceanic plate (*24*). Thus the G is associated with vertical changes in mantle azimuthal anisotropy.

For a discontinuity arising from anisotropy, the detection of the interface is dependent upon the relative orientations of the overlying and underlying fabrics,

combined with the strength of the anisotropy in each layer and the azimuthal sampling provided by source/receiver paths. As discussed in (*24*), layered changes in azimuthal anisotropy give rise to SS precursor underside reflections of varying amplitude and sign, depending upon the relative orientation of anisotropy within each layer. Despite limitations in the resolution near ridges and a lack of data sampling beneath older crust, where observed, the detections of the G reflector are tied to vertical changes in mantle anisotropy at a roughly constant depth (Fig. 2), thus requiring a compositional or dynamical component for the origin of the G over purely thermal mechanisms.

Partial melt in the LVZ can help explain observations of increased shear velocity contrast, attenuation (*10*), and mantle conductivity (*25*). Where the G roughly coincides with the top of layer 2, partial melt also offers a possible explanation for observations of layered anisotropy (*3*). Partial melt will introduce azimuthal anisotropy when mantle flow in layer 2 entrains and segregates a small fraction of melt into *en echelon* tilted layers (*26*), with fast axes aligned perpendicular to mantle flow (Fig. 3A). The presence of such a feature would result in the formation of the G at the solidus/melt interface or where there is a change in mantle permeability (*5*). In this model of the G, partial melt must be long-lived and/or dynamically renewed to sustain such structures, and thus sheared melt layers would be expected to produce persistent azimuthal anisotropy in the vicinity and downstream of sustained mantle upwellings (*24*), or in the regions of melting produced by small scale convection. This interpretation is consistent with the observed strong azimuthal anisotropy and well defined G detections near Hawaii, a long-lived mantle upwelling.

Alternatively, variable hydration with depth offers a subsolidus mechanism for producing anisotropy [e.g., (*7, 9*), Fig. 3B], although not necessarily in exclusion of tilted melt layers. The presence of 100-300 ppm $H_2O$ reduces the viscosity of olivine and modifies the mineral's anisotropic properties (*8*), readily producing fabrics at higher hydration states and elevated temperature. Dehydration of the mantle underlying the mid-ocean ridge generates a chemically depleted, viscous layer of 50 km-80 km thickness (*7*) that subsequently becomes overprinted by lowered temperatures as the plate cools and migrates away from the spreading center. This will produce alignment of the olivine SV fast axes with the paleospreading direction at the ridge, occurring primarily in the

underlying hydrated, and more deformable layer 2, producing an anisotropic discontinuity at the base of the dehydrated layer. As the lid cools and thickens, this alignment would be frozen and preserved into the part of the lithosphere (layer 1) that lies below the chemical depletion boundary, whereas flow in the warmer underlying asthenosphere (layer 2) would align with present-day APM and potentially deviate from flow at the ridge. This interpretation accounts for the anisotropy of layer 2 and for the frozen-in anisotropy observed below the G in layer 1. In this scenario, both the asthenosphere and the part of the lithosphere located below the G are hydrated, but thermal effects dominate the nature of the lid and underlying LVZ.

**Fig. 1 Lateral variations in wave velocity and anisotropy at different depths.** Mantle S-wave velocity anomalies (A-C) are given with respect to radially anisotropic PREM (*16*). Azimuthal anisotropy is plotted on top of the velocity model with black bars representing the fast $V_{SV}$ direction. Yellow arrows represent the APM obtained from no net reference frame model NNR-NUVEL 1A (*15*), and thin white lines denote ocean floor fracture zones (*27*). Thick white contour lines denote ocean floor ages at 40 Ma intervals. They are annotated in (D-F), which displays our radial anisotropy model. Other depths are shown in Fig. S26. Considering the estimated lateral resolution of the data employed, we do not resolve variations in $V_S$ or $\xi$ much smaller than 1600 km (and 5000 km for azimuthal anisotropy).

**Fig. 2 Anisotropy and velocity models as a function of oceanic crust age**. Plate-averaged A) azimuthal anisotropy amplitude, B) angular difference between $V_{SV}$ fast axes and APM directions (*15*), C) vertical gradient of fast SV axes orientation, D) S-wave velocity, and E) radial anisotropy as a function of ocean sea floor age beneath the Pacific. The black lines represent half space cooling models (*28*) assuming $T_m$=1350ºC for the mantle temperature, and $\kappa=10^{-6}$ $m^2s^{-1}$ for the thermal diffusivity. Grey dashed lines are for plate models (*29*). The temperature interval is 100ºC starting at 900ºC for the shallowest isotherm. The white circles and their standard deviations correspond to SS precursor detections of the G (*5*). Other symbols correspond to other high frequency analyses of seismic discontinuities from other groups for whom references can be found in the caption of Fig. S10.

**Fig. 3 Proposed models for azimuthal anisotropy beneath the Pacific and detection of the G**. A) The G as the top of an anisotropic entrainment and segregation of melt within the asthenosphere. Dynamical upwelling produces melt that is entrained into mantle flow and compacts at the base of the lithosphere from a solidus induced change in permeability (*10*). The G coincides with the top of the melting zone. In the scenario where the APM and fossil spreading directions are parallel, the G would not be detected. B) The G as a chemical boundary between a weakly anisotropic dry layer and a hydrated region characterized by the fossil frozen-in alignment of olivine. Olivine aligns with the present-day APM in the hydrated, warm asthenosphere. In this scenario, G can be both

coincident with and above the thermally defined LAB, and is detected by the SS precursors where the anisotropy contrast between the two layers is large.

**References:**


1. Gutenberg, B., *B Seismol Soc Am* **38**, 121 (1948).
2. Bagley, B., Revenaugh, J., *J Geophys Res-Sol Ea* **113**, (2008).
3. Kawakatsu, H. *et al.*, *Science* **324**, 499 (2009).
4. Rychert, C. A., Shearer, P. M., *J Geophys Res-Sol Ea* **116**, doi:10.1029/2010jb008070 (2011).
5. Schmerr, N., *Science* **335**, 1480 (2012).
6. Tan, Y., Helmberger, D. V., *J Geophys Res-Sol Ea* **112**, doi:10.1029/2006jb004853 (2007).
7. Gaherty, J. B., Kato, M., Jordan, T. H., *Phys Earth Planet In* **110**, 21 (1999).
8. Hirth, G., Kohlstedt, D. L., *Earth Planet Sc Lett* **144**, 93 (1996).
9. Karato, S., *Earth Planet Sc Lett* **321-322**, 95 (2012).
10. Sakamaki, T. *et al.*, *Nature Geoscience* **6**, 1041 (2013).
11. Materials and methods are available on Science online.
12. Visser, K., Trampert, J., Kennett, B. L. N., *Geophys J Int* **172**, 1016 (2008).
13. Debayle, E., Ricard, Y., *Earth Planet Sc Lett*, (2013).
14. Yuan, H. Y., Romanowicz, B., *Nature* **466**, 1063 (2010).
15. Gripp, A. E., Gordon, R. G., *Geophys J Int* **150**, 321 (2002).
16. Dziewonski, A. M., Anderson, D. L., *Phys Earth Planet In* **25**, 297 (1981).
17. Maggi, A., Debayle, E., Priestley, K., Barruol, G., *Geophys J Int* **166**, 1384 (2006).
18. Nettles, M., Dziewonski, A. M., *J Geophys Res-Sol Ea* **113**, doi:10.1029/2006JB004819 (2008).
19. Nishimura, C. E., Forsyth, D. W., *Geophys J*+ **96**, 203 (1989).
20. Karato, S., in *High-Pressure Research in Mineral Physics,* Mangh- nani, M. H., Syono, Y., Eds. (TERRAPUB/AGU, Tokyo/Washington, 1987), pp. 455-471.
21. Miyazaki, T., Sueyoshi, K., Hiraga, T., *Nature* **502**, 321 (2013).
22. Hager, B. H., Richards, M. A., *Philos T Roy Soc A* **328**, 309 (1989).
23. Gaboret, C., Forte, A. M., Montagner, J. P., *Earth Planet Sc Lett* **208**, 219 (2003).
24. Rychert, C. A., Schmerr, N., Harmon, N., *Geochem Geophy Geosy* **13**, (2012).
25. Naif, S., Key, K., Constable, S., Evans, R. L., *Nature* **495**, 356 (2013).
26. Holtzman, B. K., Kendall, J. M., *Geochem Geophy Geosy* **11**, (2010).
27. Matthews, K. J., Muller, R. D., Wessel, P., Whittaker, J. M., *J Geophys Res-Sol Ea* **116**, (2011).
28. Parker, R. L., Oldenburg, D. W., *Nat Phys-Sc* **242**, 137 (1973).
29. Stein, C. A., Stein, S., *Nature* **359**, 123 (1992).



**Acknowledgements:** CB and KY were funded by NSF EAR grants number 0838605 and 0949255; NS was funded by NSF EAR 1247608. The authors thank Jeannot Trampert and Karin Visser for making their phase velocity maps freely available. Partial derivatives were calculated using fortran code MINEOS (http://www.geodynamics.org/cig/software/mineos), and figures were made using the Generic Mapping Tools, Gnuplot, and Xmgrace. We thank Paul Davis for fruitful

discussions. The data employed were the phase velocity maps published in (*12*) and are available on Jeannot Trampert's website. The models are available at http://www2.epss.ucla.edu/~cbeghein/BYSX14.tar.gz

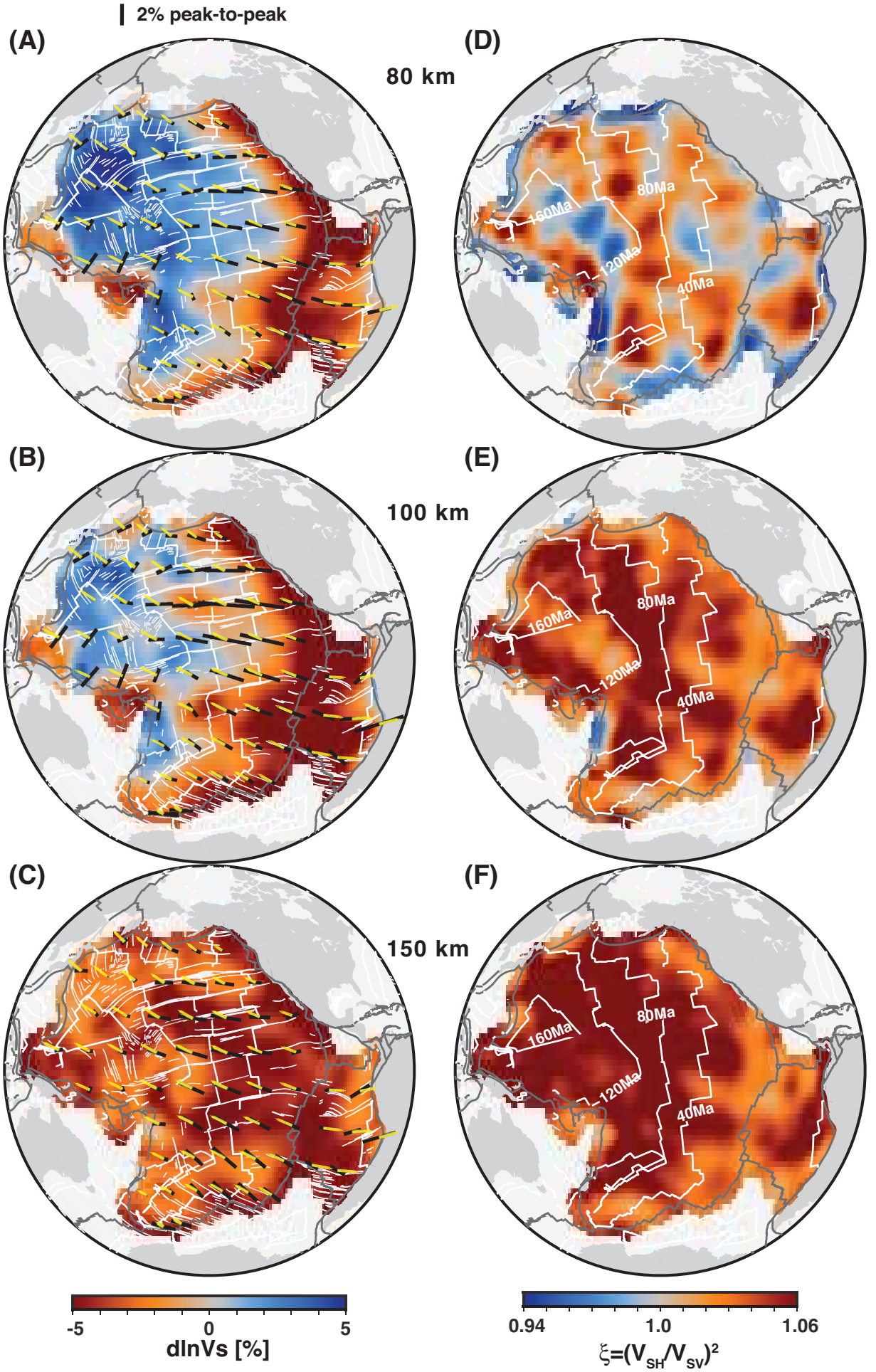
2% peak-to-peak
(A)
80 km
(D)
160Ma
80Ma
120Ma
40Ma
(B)
100 km
(E)
160Ma
80Ma
120Ma
40Ma
(C)
150 km
(F)
160Ma
80Ma
120Ma
40Ma
-5
0
5
dlnVs [%]
0.94
1.0
1.06
ξ=(V_SH/V_SV)²

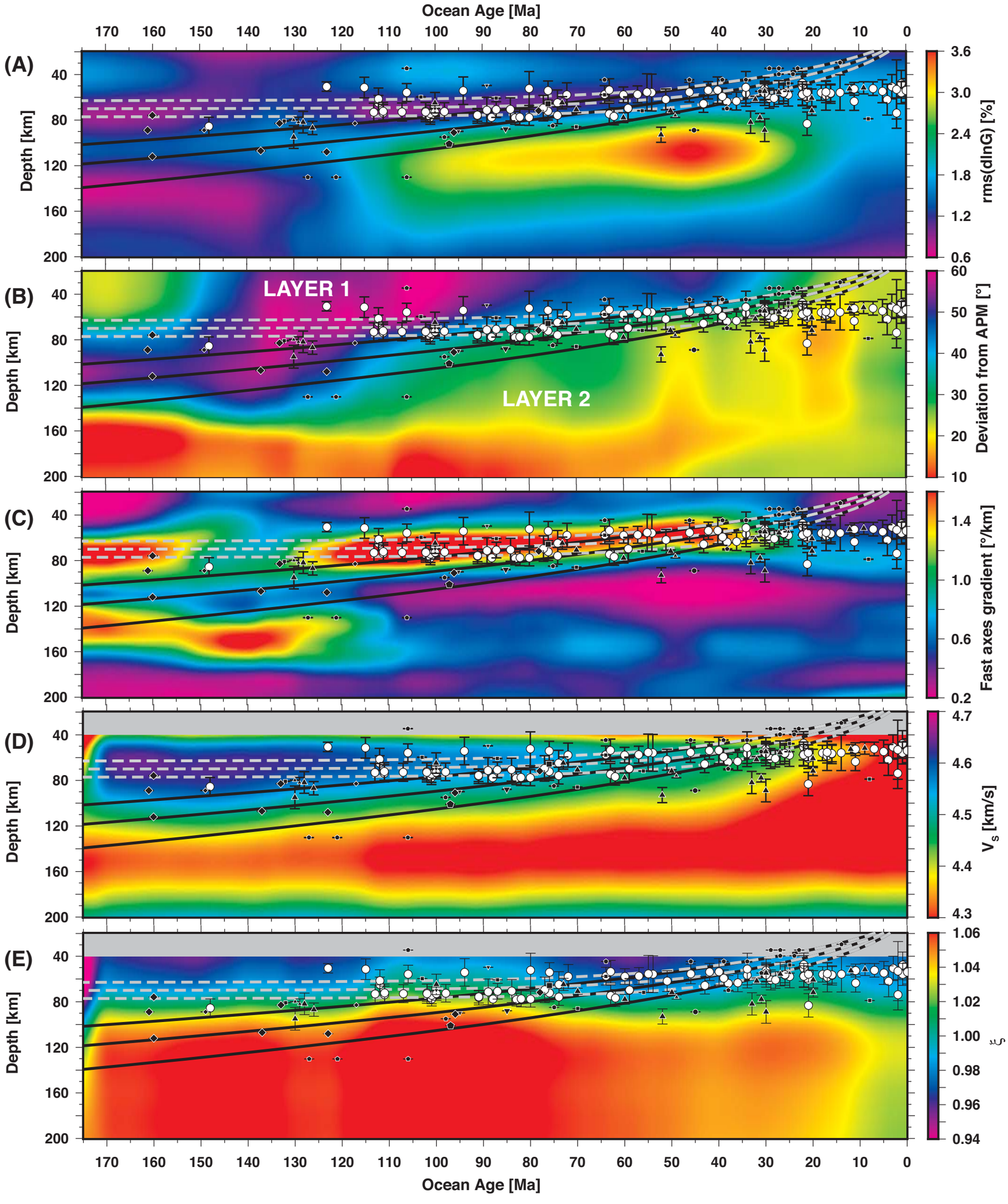
Ocean Age [Ma]
170 160 150 140 130 120 110 100 90 80 70 60 50 40 30 20 10 0
(A)
(B)
(C)
(D)
(E)
Depth [km]
40 80 120 160 200
LAYER 1
LAYER 2
rms(dlnG) [%]
3.6 3.0 2.4 1.8 1.2 0.6
Deviation from APM [°]
60 50 40 30 20 10
Fast axes gradient [°/km]
1.4 1.0 0.6 0.2
V_S [km/s]
4.7 4.6 4.5 4.4 4.3
ξ
1.06 1.04 1.02 1.00 0.98 0.96 0.94

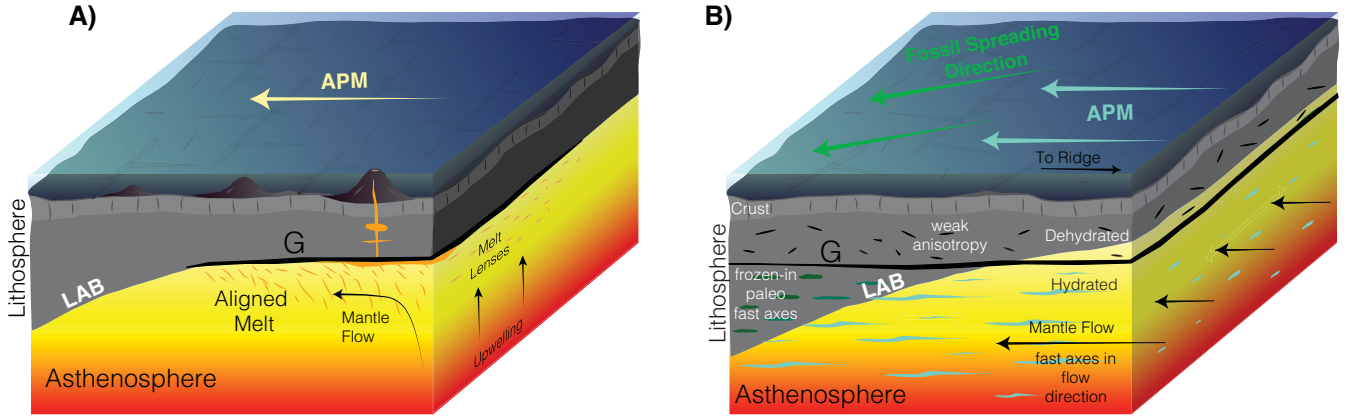
A)
APM
Lithosphere
G
LAB
Aligned
Melt
Mantle
Flow
Melt
Lenses
Upwelling
Asthenosphere
B)
Fossil Spreading
Direction
APM
To Ridge
Crust
weak
anisotropy
Dehydrated
Lithosphere
G
frozen-in
paleo
fast axes
LAB
Hydrated
Mantle Flow
fast axes in
flow
direction
Asthenosphere